

Nano-scale stoichiometry analysis of a high temperature superconductor by atom probe tomography

S. Pedrazzini¹, A. J. London¹, B. Gault^{1,2}, D. Saxey³, S. Speller¹, C. R. M. Grovenor¹, M. Danaie¹, M. P. Moody¹, P. D. Edmondson⁴, P. A. J. Bagot¹

¹ *Department of Materials, University of Oxford, Parks Road, OX1 3PH, Oxford, UK.*

² *Max Planck Institute für Eisenforschung, Max-Planck-Straße 1, 40237 Düsseldorf, Germany.*

³ *Geoscience Atom Probe, Advanced Resource Characterisation Facility, John de Laeter Centre, Curtin University, Perth, WA 6102, Australia.*

⁴ *Materials Science & Technology Division, Oak Ridge National Laboratory, 1 Bethel Valley Road, Oak Ridge, TN 37831, Tennessee, USA.*

Abstract

The functional properties of the high temperature superconductor $\text{Y}_1\text{Ba}_2\text{Cu}_3\text{O}_{7-\delta}$ (Y-123) are closely correlated to the exact stoichiometry and oxygen content. Exceeding the critical value of 1 oxygen vacancy for every 5 unit cells ($\delta > 0.2$, which translates to a 1.5 at.% deviation from the nominal oxygen stoichiometry of $\text{Y}_{7.7}\text{Ba}_{15.3}\text{Cu}_{23}\text{O}_{54-\delta}$) is sufficient to alter the superconducting properties. Stoichiometry at the nanometre scale, particularly of oxygen and other lighter elements, is extremely difficult to quantify in complex functional ceramics by most currently available analytical techniques. The present study is an analysis and optimisation of the experimental conditions required to quantify the local nano-scale stoichiometry of single crystal yttrium barium copper oxide (YBCO) samples in 3D by Atom Probe Tomography (APT). APT analysis required systematic exploration of a wide range of data acquisition and processing conditions to calibrate the measurements. Laser energy, ion identification and the choice of range widths were all found to influence composition measurements. The final composition obtained from melt-grown crystals with optimised superconducting properties was $\text{Y}_{7.9}\text{Ba}_{10.4}\text{Cu}_{24.4}\text{O}_{57.2}$ at.%.

1. Introduction

Yttrium Barium Copper Oxide (YBCO) is one of the most commonly studied high temperature superconductors with potential applications in large-scale power generators (Takeuchi, Amemiya, Nakamura, Maruyama, & Ohkuma, 2011) and ac power transmission cables (Li, Amemiya, Takeuchi, Nakamura, & Fujiwara, 2011). It has also been proposed as a candidate material for the magnetic confinement of plasma in Tokamak reactors (Sykes et al., 2014). Its chemical formula is $\text{Y}_1\text{Ba}_2\text{Cu}_3\text{O}_{7-\delta}$ (Y-123), where δ is a parameter describing the formation of vacancies on the oxygen sub-lattice controlled by the valence state of the metallic Cu (II)/Cu (III) ions (Jorgensen et al., 1991). The value of δ can be used to predict the functional properties of the material. When $\delta=0.5$ the triple-layer perovskite phase has tetragonal symmetry (Degardin et al., 2014; Kreisler, Jagtap, Sou, Klisnick, & Degardin, 2012). A tetragonal-to-orthorhombic phase transition occurs at $\delta \sim 0.2$ (i.e. no more than 1 oxygen site for every 5 unit cells can be vacant for the orthorhombic crystal structure to be stable). Superconductivity is exhibited by this orthorhombic phase (Benzi, Bottizzo, & Rizzi, 2004). As the value of δ decreases further, between $0.2 \geq \delta \geq 0$, the superconducting transition temperature increases from ~ 60 K up to a maximum of 90 K (Benzi et al., 2004). Therefore the desired crystal structure and functional properties of YBCO depend on an extremely delicate balance of oxygen stoichiometry and vacancies on the oxygen sub-lattice.

Non-stoichiometry in the oxygen sub-lattice is of crucial importance to the electrical properties of a wide range of complex functional oxide materials but has proved extremely difficult to quantify on the nanoscale (Badwal, Giddey, Munnings, & Kulkarni, 2014; Chen, Bishop, & Tuller, 2013; Jia, Lentzen, & Urban, 2003; Seh, Fritze, & Tuller, 2007; Tuller & Bishop, 2011). Finding a reliable way to quantify local oxygen stoichiometry is essential for the prediction of the properties of functional oxides e. g. strontium titanate (STO), materials such as YBCO and other high temperature oxide superconductors in real service environments. Previous studies have attempted to measure (or to estimate) the oxygen content of YBCO using a variety of experimental approaches. Some estimates rely on indirect methods, such as the measurement of the c-axis unit cell dimension, which depends on the value of δ (Benzi et al., 2004; Degoy et al., 1996; Wu et al., 1998). Alternatively, bulk oxygen measurements are relatively quick and easy, providing average values of δ . Most such methods involve the extraction of oxygen from the sample using dissolution and a chemical method to calculate the oxygen content. Examples are the reduction of samples in a hydrogen flow (Graf, Triscone, & Muller, 1990), iodometric titration (Benzi et al., 2004) or spectrophotometry – which involves dissolution of YBCO in acid solvents then wavelength absorbance measurements (Nedeltcheva, 1995; Nedeltcheva & Vladimirova, 2001). These methods provide an average value of oxygen content over large sample volumes, giving no indication of localised segregation effects nor the distribution of point defects, and are likely insufficient for property predictions unless the sample is microscopically and macroscopically uniform.

Localised, nano-scale Transmission Electron Microscopy (TEM) based observations have always been significantly more challenging due to the low scattering factor of O atoms. In 2003, there was a breakthrough by Jia *et al.* who used aberration corrected TEM on YBCO and STO samples to observe the individual atoms in each lattice site, including oxygen (Jia et al., 2003). In recent years, developments in instrumentation and analytical techniques have made HRTEM studies more common on YBCO samples (Suvorova et al., 2014). Such measurements allow oxygen columns to be resolved on an atomic scale in two-dimensional projections down various zone axes, but oxygen vacancies remain hard to detect within columns of oxygen atoms.

One of the only techniques so far which has the capability to detect nano-segregation in 3D and local variations in oxygen content in YBCO is Atom Probe Tomography (APT). APT is based on the concept of field evaporation, and combines time-of-flight mass spectrometry with a position sensitive detector to reconstruct a 3D image of samples with near-atomic resolution. Previous studies can be found in the scientific literature pertaining to nano-scale analysis of YBCO through field emission techniques (Cerezo, Grovenor, Hoyle, & Smith, 1988; Kellogg & Brenner, 1987; Melmed, Shull, Chiang, & Fowler, 1988; Nishikawa & Nagai, 1988). These studies were undertaken in the 1980s using either a 1D atom probe or a field ion microscope (FIM). FIM was used to attempt superconductivity measurements by comparing the evidence concerning preferential evaporation in superconducting samples when compared to insulating samples at 50 K (Melmed et al., 1988). Localised chemical composition measurements were restricted to very small one-dimensional analysis volumes. The detected compositions were deficient from the nominal oxygen content of the fully oxygenated perovskite, the closest measurement being deficient by more than 3 at.% O (Cerezo et al., 1988). More recent developments in APT instrumentation and analytical tools include reflectron lenses (Clifton, Gribb, Gerstl, Ulfig, & Larson, 2008) that allow for substantial improvements in the precision of chemical analysis, the implementation of laser pulsing (Bunton, Olson, Lenz, & Kelly, 2007; Cerezo et al., 2007; Deconihout et al., 2007) and local electrodes (Kelly & Larson, 2000), which allow the analysis of a much greater sample volume from a wider range of compound materials and the use of a Focussed Ion Beam (FIB) microscope for sample preparation (Kelly & Larson, 2000; Thompson et al., 2007) which enables the site-specific analysis of individual selected features. In addition sophisticated post-acquisition analytical tools such as multiple hit correlation histograms (Saxey, 2011) can now be used to correct for aberrations and artefacts.

The present study makes use of all these advances, along with a systematic study of experimental conditions to provide accurate measurements of 3D nanoscale oxygen stoichiometry on bulk samples of the perovskite superconductor YBCO, and discusses the wider implications of this work for experiments on a wider range of functional oxide materials.

2. Experimental Methods

Single crystal YBCO samples, provided by the bulk superconductivity group in the Cambridge University Engineering Department, were produced by the Top Seeded Melt Growth (TSMG) process (Babu et al., 2012). Powders of the required compositions were pressed into a compact pellet, followed by partial melting and peritectic regrowth of the $\text{Y}_1\text{Ba}_2\text{Cu}_3\text{O}_{7-\delta}$ phase (Y-123). A chemically stable $\text{GdBa}_2\text{Cu}_3\text{O}_7$ seed was used as a heterogeneous nucleation site for epitaxial growth of a large Y-123 single crystal. An excess of 20-30% of $\text{Y}_2\text{Ba}_1\text{Cu}_1\text{O}_5$ phase (Y-211) particles was included in the starting powder as inclusions to produce pinning sites for magnetic flux lines to enable superconductivity (Murakami et al., 1991). 1 wt.% of CeO_2 has also been added to refine the Y-211 particles during the melt process, which is known to result in a significant increase in flux pinning strength and consequent improvement in superconducting properties (Kim et al., 1992; Pinol et al., 1994). The mechanism responsible for this refining effect is not fully understood, but may involve the solid-state formation of Y_2O_3 nanoparticles that act as nucleation sites for small Y-211 particles (Vilalta, Sandiumenge, Pinol, & Obradors, 1997).

Superconductivity temperature measurements were performed using a Quantum Design SQUID (Superconducting Quantum Interference Device), oriented with the applied field $B//\langle a \rangle$ axis. Measurements were performed at constant field, varying the temperature and measuring the corresponding variation in magnetic moment.

Bulk samples were cut from these crystals along the crystallographic $\langle a \rangle$ axis (the unit cell is shown in Figure 1a) and polished to a 1 μm diamond finish using ethanol as a lubricant to avoid decomposition of the YBCO. Secondary electron micrographs were acquired using a Zeiss NVision 40 dual beam scanning electron microscope – focussed ion beam (SEM – FIB). Site specific samples were prepared for APT analysis using the FIB lift-out technique from a region containing both Y-123 matrix and Y-211 particles (Thompson et al., 2007). Triangular sections were mounted onto Cameca silicon sample holders (coupons) for APT analysis and sharpened until the tip diameter was <100 nm. Gallium damage was minimised by reducing the voltage from 30 to 5 kV.

A Cameca LEAP 3000X HR was used for atom probe analysis. Samples were laser pulse evaporated, with a pulse frequency of 160 kHz, at a sample temperature of 50 K. The choice of laser energy is well known to influence the analysed stoichiometry of non-metallic samples such as oxides (Bunton et al., 2007; La Fontaine et al., 2015) and was deemed to be one of the key variables requiring optimisation in this work. One sample was therefore used for a calibration experiment, in which the laser energy was systematically changed over a range 0.05-0.6 nJ/pulse, with at least 600,000 ions captured at every setting, with the evaporation rate maintained at 0.7%. To ensure consistency, the starting point and finishing point of the experiment were both 0.4 nJ.

Analysis of the data sets was performed in part using the standard Cameca IVAS 3.6.6 software and partly by converting the data files to the IVAS extended position file (epos) format, which provides additional outputs characterising each reconstructed ion, including: instantaneous voltage, reconstructed x, y, and z coordinates, time of flight and whether an ion is detected as a single event or was one of multiple detected ions triggered by the same laser pulse. Matlab (Mathworks) and C++ scripts custom written for the present analysis were used to read the outputs, to perform background corrections, to read the number of multiple hits at each laser energy, to analyse the effect of different range widths on chemical composition and to plot multiple hit correlation histograms.

3. Results

The TSMG process produced a microstructure consisting of discrete Y-211 particles $<5\mu\text{m}$ in diameter within the single crystal Y-123 matrix, as shown in a typical SEM micrograph in Figure 1b. SQUID magnetisation measurements on a 3 mm diameter sample of the analysed material showed a sharp decrease in magnetisation signal at 90 K, confirming that the superconducting Y-123 phase is fully oxygenated. The fact that these melt-grown crystals have excellent superconducting properties (as shown in Figure 1c) provides confidence in their chemical composition. It is possible, though unlikely, that the sample composition as measured by APT could have been affected by the FIB-based specimen preparation procedure. Hence, low voltage final-stage milling

was performed in the FIB to minimise the Ga-affected volume and a separate initial data set was collected from the same sample until Ga contamination was no longer detectable by APT.

Data from an APT sample containing an Y-211 particle is shown in Figure 2 (a), allowing the interface between Y-211 and the surrounding Y-123 matrix to be analysed. Y-211 particles are electrical insulators, which makes them more likely to fracture when subjected to the electric fields generated at the sample tip in the atom probe. For this reason, the sample yielded a relatively small data set (300,000 ions), making it unsuitable for calibration analysis of the effect of experimental parameter variation on the chemical composition.

The mass spectrum did however contain sufficient ions to confirm that at 0.4 nJ the expected Y:Ba:Cu:O ratios of 2:1:1:5 in the Y-211 phase and 1:2:3:7 in the Y-123 phase both deviated slightly from the expected stoichiometries due to minor Ba and O deficiencies. The chemical composition profile across the Y-123 and Y-211 phases measured as a function of distance from the interface is shown in Figure 2 (b). No Ce was detected within the Y-211 phase, the Y-123 phase or at the interface between them (however due to the small data set, counting errors were comparatively large at ± 0.15 at.%, which may have prevented the detection of Ce, if present below this threshold).

Theories suggests that the mechanism of refinement of Y-211 particle size involves the formation of Y_2O_3 nanoparticles in solid state reactions between the superconducting matrix and Y-211 and CeO_2 to form BaCeO_3 (Vilalta et al., 1997). In the present data set no evidence of Y_2O_3 was found.

The APT analytical conditions were optimised on a much larger 17 million-ion data set collected wholly from the Y-123 matrix. A plot summarising the experimental conditions across the course of this analysis is shown in Figure 3 (a). The laser pulsing energies and resulting voltage adjustments (to maintain a constant ions-detected-per-pulse detection rate) were plotted as a function of the instantaneous total number of ions detected during the calibration experiment. The applied voltage directly determines the intensity of electric field to which the sample is exposed. If the field changes, the distribution of charge-states at which ions are detected will change as a result. As such the charge-state ratios, i.e. the ratio of the detected frequency of different charge states of the same type of ion, can be used an approximate metric to quantify the electric field. Therefore the charge state ratios for every ion were plotted as shown in Figure 3 (b). As expected increasing laser energy, thereby reducing the applied electric field, results in a relative increase in the detection of lower charge states. The reconstruction of the calibration sample is shown in Figure 4 (a).

This data set was used to calibrate the experimental conditions. It is assumed that the analysis volume incorporated by Figure 4 (a) ($\sim 80 \text{ nm} \times 80 \text{ nm} \times 300 \text{ nm}$) is homogeneous $\text{Y}_1\text{Ba}_2\text{Cu}_3\text{O}_{7-\delta}$. Note that no abrupt changes in local ion density or apparent composition are detected the data set in Figure 4 (a) as the laser energy is changed. Figures 4 (b) and (c) superimpose the normalised mass spectra at the lowest and highest energies, 0.05 nJ and 0.6 nJ, respectively. A close-up of a section of the mass spectra, between 30 and 38 Da, illustrates specific differences in mass resolution resulting from changes to the applied laser energy. The mass spectra shown were normalised using the O_2^+ peak at 32 Da, which was the highest peak in both spectra.

4. Discussion

The following discussion and analysis the based on the presumption that the chemical composition of bulk superconducting crystal samples is close to the nominal stoichiometry of the $\text{Y}_1\text{Ba}_2\text{Cu}_3\text{O}_{7-\delta}$ compound, which is 7.7 at.% Y, 15.3 at.% Ba, 23.1 at.% Cu and 53.9 at.% O, assuming $\delta \rightarrow 0$. This claim was substantiated by the excellent superconducting properties previously shown in Figure 1c. Further factors, such as analytical conditions, which can influence the accuracy of chemical composition and stoichiometry measured through APT are analysed and discussed in the following sections. An interesting future development would include a round robin experiment in order to establish how that impacts the comparison of data from different instruments and different labs if we are to make quantitative comparisons on the same materials, such as the recent work performed by Marquis *et al.* (Marquis et al., 2016).

4.1 Ion identification and defining the width of each peak in the mass spectrum that will maximise signal to noise ratios (range width)

The stage of the analysis procedure that has the greatest influence on the apparent sample composition is ion identification and setting range widths (Hudson, Smith, & Gault, 2011). From the typical mass spectra collected Y^+ , Ba^{2+} , Cu^{2+} and O^+ mono-atomic ions were identified as well as a large number of complex molecular-ions, including YO^+ , YO^{2+} , CuO^+ , CuO^{2+} , $YCuO^+$ and $YCuO_2^+$ as well as O_2^+ . Based on previous studies of oxide samples (Bachhav, Danoix, Hannover, Bassat, & Danoix, 2013), the peak at 16 Da was considered not to have any significant contributions from O_2^{2+} ions. In an effort to minimise mass spectrum peak identification errors, the same mass spectrum was ranged independently by two of the authors. Both ranging efforts were found to be consistent in terms of ion selection. Other parameters, such as widths will be discussed in the next sections.

Choices of range widths can also make significant differences to measured chemical compositions, though to a smaller extent than ion identification. No universally applicable ranging standards are available, however, some dedicated studies can be found in the literature. Hudson *et al.* performed systematic analyses on trace elements in Zr samples and concluded that ranging the full width nine-tenth maximum of each peak provided the analysed composition closest to the nominal value (Hudson *et al.*, 2011). La Fontaine *et al.* established that the difference between the two extreme ways of ranging (from full-width-nine-tenth-maximum to background-to-background) were equivalent within the error bars for oxidised stainless steel (La Fontaine *et al.*, 2015). The compositions measured using several different methodologies in the present work are shown in Table 1.

Assuming that the volume of material analysed in this experiment has the nominal fully oxygenated composition $Y_1Ba_2Cu_3O_7$ the metal composition is most accurate when background-to-background ranging is applied, while the oxygen content accuracy is improved when the full-width-nine-tenth-maximum approach is followed.

If all the peaks had the same shape and width then the composition would be independent of range width. The difference in composition measured with different range widths is a result of the asymmetry of the peaks, due to the thermal tails and the changes in peak widths corresponding to different ions. The peak width in laser-assisted measurements will depend on the field required to evaporate each ionic species from the sample apex (Gault, Moody, Cairney, & Ringer, 2012). This effect causes the peaks to change across the reconstruction. The selected widths are therefore not tailored to a specific experimental condition but are being applied to the average of a range conditions. i.e. the best performing ranging approach is effectively the most robust across the changing field conditions. Because no information could be obtained for the evaporation field of every type of ion detected in the present mass spectra, as a compromise, full-width-half-maximum was selected for the following analysis. The measured chemical composition from the whole atom probe run at the selected range width was $Y_{7.4}Ba_{16.2}Cu_{23.8}O_{52.4}$ at.% and contained traces of ~ 0.17 at.% Ce, whereby Ce was identified as the CeO^{2+} peak at 78 Da.

4.2 Thermal tails

Samples which are thermally insulating when illuminated with a laser pulse will dissipate heat more slowly. As a result, the specimen remains at a higher temperature for a longer time, and hence the field evaporation process can continue for several ns after the application of each laser pulse (Bunton *et al.*, 2007). This delayed evaporation manifests in the acquired time-of-flight spectrum as a “thermal tail” which extends from the main peak to longer times. When the time-of-flight spectrum is converted into a mass-to-charge spectrum, this effect is evident through tails which extend from the main peak to higher effective masses. During analysis of the spectrum, thermal tails can raise the effective noise level and hide smaller peaks, potentially causing the introduction of errors into any chemical quantification. Figure 4 (b) clearly illustrates a reduction of thermal tail size in the whole spectrum when the laser energy is reduced. Figure 4 (c) shows the small $^{65}Cu^{2+}$ peak just after the large O_2^+ peak, which at higher laser energies would be hidden in the thermal tail. This demonstrates that for the present samples a reduction in laser energy from 0.6 nJ to 0.05 nJ can lead to an effective improvement in mass resolution, and hence more confidence in the ranging of the mass spectrum.

This effect can be explained as the reduction in laser energy is expected to lead to a lower maximum temperature reached at the sample apex. The temperature change caused by the laser has been both experimentally estimated and modelled in previous studies on a variety of materials (Liu & Tsong, 1984), and is known to be dependent upon the laser energy and the individual specimen properties (Kelly et al., 2014; Liu & Tsong, 1984). If the maximum temperature is reduced, the time required for the surface to quench will also decrease. This, in turn, will cause ion evaporation to occur within a narrower time range after each individual pulse, reducing the “tail” effect in both the time-of-flight spectrum and therefore also in the final mass spectrum.

4.3 Effect of Laser Energy

The effect of altering laser energy on composition is shown in Figure 5 (a). Each data point represents a 600,000 ion sections of the 17 Million ion data set. The entire Ba content of the analysed volume was detected in the form of Ba^{2+} ions at 65-69 Da, which was expected based on the post-ionisation theory developed by Haydock and Kingham (Gault et al., 2012). However this also means that the overlap with the thermal tail of the Cu^+ ions at 63 and 65 Da (Figure 5 (b)) can cause an overestimate of the Ba content of the sample. The compositions given in Figure 5 (c) were therefore background corrected by fitting an exponentially decaying function to the thermal tails and subtracting them using a custom Matlab code developed by London *et al.* (London et al., 2015). London et al developed a model fitting for the peaks in their mass spectrum, by using an exponentially corrected Gaussian function for the peak shape, with an added exponentially decaying function on one side as the thermal tail, as described in further depth in their paper (London et al., 2015). At a laser energy below 0.25 nJ, the overall composition of the sample is approximately constant, but a significant Ba deficiency is seen at every laser energy, as seen in Figure 5 (b).

One suggested reason for the measured Ba deficiency could be correlated to its lower evaporation field when compared to Cu or Y (Gault et al., 2012) (however it is important to note that evaporation fields of elements have only been measured in their elemental state, they could be different in the case of compounds). Barium could be field-evaporating throughout the experiment in a way which is uncorrelated with the laser pulses. In this case the ions would leave the tip and reach the detector, however their time-of-flight could not be measured and they would therefore be unidentifiable, hidden in the mass spectrum background noise. This suggestion is further supported by the evidence presented in Figure 5 (b), which proves that at higher laser energies (which means lower applied voltage, therefore lower field) more Ba is detected.

Further evidence supporting this theory is provided by the raise in background rate with decreasing laser energy. The background rate was measured in a region where no peaks or thermal tails were present, therefore between 4-11 Da. At low laser energy (between 0.05- 0.15 nJ) the background rate was 8.1×10^{-5} /amu, while at high laser energy (between 0.45-0.6 nJ) it was 7.6×10^{-5} /amu when measured on a dataset divided into bins of 0.05 Da. The background rate showed an effective increase by 6% at lower laser energy, which can be indicative of off-pulse evaporation by one or more chemical species.

4.4 Event multiplicity

Multiple events occur when two or more ions reach the detector that are correlated to application of the same laser or voltage pulse. A simple custom program was written in C++ to extract the number of multiple events from the .epos files and plot them as a function of laser energy. The output is shown in Figure 6.

Figure 6 shows that the proportion of multiple hits decreases from 0.47 to 0.38 when the laser energy is increased from 0.05 nJ to 0.6 nJ. As previously discussed by Tang *et al.* (Tang, Gault, Ringer, & Cairney, 2010) multiple events can represent a detection challenge. The analysis of thermally and electrically conductive samples will typically show high single-to-multiple event ratios, e.g. ~0.95 for a pure Al specimen. In comparison, in a recent study of gallium nitride, a covalently bonded, semiconducting thermal insulator, after optimising the laser energy a ratio of 0.41 was observed. This is similar to the ratios observed in the present work.

This ratio is important because when more than one ion, triggered by the same laser pulse, arrive at the detector, algorithms are implemented which investigate all the possible combinations of the acquired signals on the delay-line detectors. The aim is deconvolute the individual contribution to the signal from each ion

and thereby estimate the most likely ‘correct’ positional information of every ion. However, as the number of multiple hits increases, so does the probability of failure of one or more of those algorithms. This can be detrimental to the precision of the composition measurement due to preferential detection-loss of certain ionic species (Tang et al., 2010). The other issue is the detector deadtime, which is about ~4 ns. If multiple events occur within this time frame, then the second ion would be undetected. Therefore in the case of multiple events, a combination of software and hardware issues cause detection challenges (Tang et al., 2010). In the present case, decreasing the laser energy improves mass resolution (as defined above) however to maintain the detection rate it also results in a more intense electric field being applied to the specimen. This is expected to be the cause of the increase in multiple events, increasing the uncertainty of the measurement.

4.5 Ion dissociation

Another factor which can influence compositional accuracy can arise due to the dissociation of complex molecular ions in the electric field en route to the detector. This dissociation can result in the formation of “neutral” species. Due to their lack of charge these neutral species may not acquire significant kinetic energy from the applied voltage to be successfully registered by the detector. Furthermore, they are more likely than their charged counterparts to take on trajectories beyond the field of view of the detector. In both cases the neutral species would not be detected and hence would not contribute to the measurements. A recent study demonstrated that the formation of the neutral molecules can result in significant loss of compositional accuracy (Gault et al., 2016).

In order to assess whether this effect is significant in the current study, multiple hit correlation histograms (Saxey, 2011) were produced for datasets corresponding to high, medium and low laser energies (dividing the data set into three equal parts), and are shown in Figure 7 (a). In this case, the data is read by a Matlab script in a 3 column format, which includes, for each entry, the laser energy, first hit mass-to-charge-state ratio (m/z) and 2nd hit m/z . These histograms plot the respective mass-to-charge-state-ratio of each pair of ions in a multiple hit event. The resulting distribution can be indicative of physical processes during field evaporation of specimen. For example the prominent diagonal lines can be explained by the delayed evaporation of both ions with respect to application of the laser pulse. These plots can also be used to identify mid-flight ion dissociation events, some of which can potentially lead to the systematic “loss” of chemical species (Saxey, 2011). This technique was first pioneered by Saxey in 2011 (Saxey, 2011) on GaN samples in a LEAP 3000X Si, where the ions are ionised, leave the tip of the sample and follow a straight flight path directly to the detector. The present work was however performed on a LEAP 3000X HR equipped with a reflectron lens, which improves mass resolution by deflecting the ion flight path differently according to their atomic weight. Figure 7 (b) shows the different ways in which ion dissociation is visible in a reflectron atom probe, when compared to a straight flight path atom probe on the same GaN sample. When the ions are deflected through a reflectron lens, the full ion dissociation track is no longer visible, and is replaced by an ellipsoidal trace with negative slope.

Ellipsoidal traces with negative slope are visible in the YBCO data shown in Figure 7 (a), and are indicative of mid-flight ion dissociation (highlighted by the arrows). This is because the time that it takes daughter ions of the dissociation to reach the detector is either increased or reduced, because of the time spent in flight in the early stages of their trajectories as part of a larger complex ion with a different over-all mass-to-charge-state. Generally the daughter ion with smaller mass-to-charge-state will arrive later than expected. Hence, the mass-to-charge-state ratio measured in the APT experiment for these ions will be distorted to larger values. The opposite is true for the daughter ion with the larger mass-to-charge-state ratio. Figure 7 provides possible evidence for dissociation occurring more at the lowest laser energies as expected since the applied voltage is higher and therefore the local field at the specimen tip is greater and the number of multiple events is higher (as shown in Figure 6). For instance, The mass-to-charge state value of the multiple events suggests that the molecular ion Cu_2O^{2+} dissociates into CuO^+ and Cu^+ , but neither of those ions would be lost as they are both charged. No other ion dissociation events were evident from the correlation histograms. This suggests that the loss of individual species due to ion dissociation should not be a problem in the present analysis.

5. Summary and conclusions

The present study has proved that atom probe tomography can be used to measure chemical compositions (and in particular oxygen stoichiometry) in the superconducting perovskite YBCO, though the interpretation of the results requires a detailed and systematic standardisation of the experimental parameters. Ion identification and range widths proved to have a substantial effect on chemical composition, and the use of full-width-half-maximum ranges were found to be most accurate in the present work.

Decreasing the laser energy was shown to improve the mass resolution by decreasing thermal “tails” in the mass spectra and improving the visibility of smaller peaks. Due to the improvement in mass resolution, the oxygen and copper content could be measured more accurately. There is however a trade-off: mass resolution is improved with decreasing laser energy but, likely due to its low evaporation field, some evidence suggests that Ba could be evaporating off-pulse. The barium content was therefore more accurate at higher laser energies. The reduced detectability of Ba due to off-pulse evaporation artificially inflates the measured content of the other elements, when expressed in units of at.%.

It is also noteworthy that the number of multiple events increased with decreasing laser energy, which increases the uncertainty of the measurement. An intermediate value of 0.3-0.4 nJ is therefore suggested for the study of YBCO. The detection loss of neutral species due to complex ion dissociation was not observed to be an issue at any of the laser energies tested.

Background corrections were required due to the insulating nature of the sample, which caused field evaporation to continue even after the laser pulse, translating in the mass-to-charge state spectrum as thermal “tails” extending from the peaks. The thermal tails were fitted to exponentially decaying functions which were then subtracted from overlapping peaks.

The final measured composition obtained was $\text{Y}_{7.9}\text{Ba}_{10.4}\text{Cu}_{24.4}\text{O}_{57.2}$ at.%. For data sets exceeding 1M ions the counting error should be small enough to allow the composition to be accurate within ± 0.01 at.%. This opens up new prospects for studying the local chemistry of nano-scale defects created by radiation damage, and explaining their influence on the superconducting properties.

Acknowledgements:

Dr. Daniel Haley is gratefully acknowledged for helping with a part of the Matlab script and the C++ program used in the present work. Dr. Tayeb Mousavi is gratefully acknowledged for performing the superconductivity measurements. Funding is acknowledged from the UK’s Engineering and Physical Sciences Research Council (EPSRC) under grant EP/K029770/1. PDE also acknowledges support from the U. S. Department of Energy, Office of Science, Fusion Energy Sciences. We would also like to thank the Bulk Superconductivity Group in the University of Cambridge for providing the samples which were used in the present study.

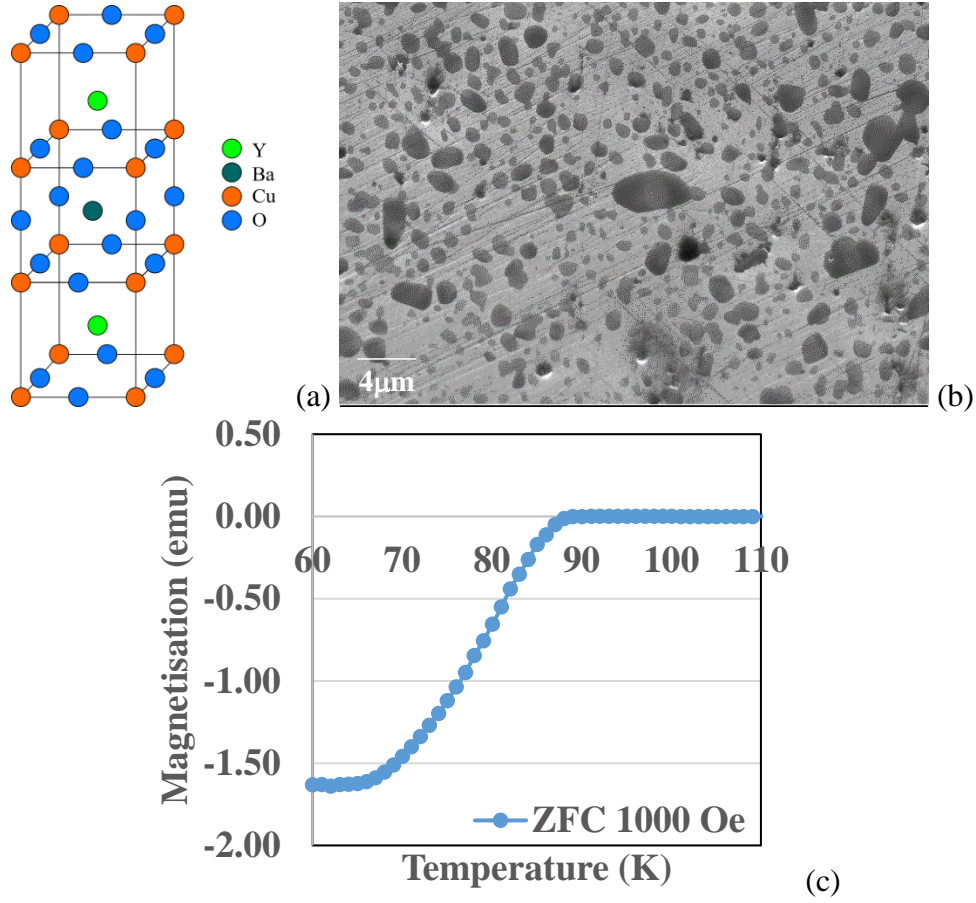


Figure 1: (a) Schematic drawing of the YBCO unit cell, (b) secondary electron micrograph showing the distribution of Y-211 particles (darker) within the Y-123 single grain matrix, as viewed along the $\langle a \rangle$ axis, (c) superconductivity measurements showing a sharp transition at 90K, typical of the fully oxygenated perovskite.

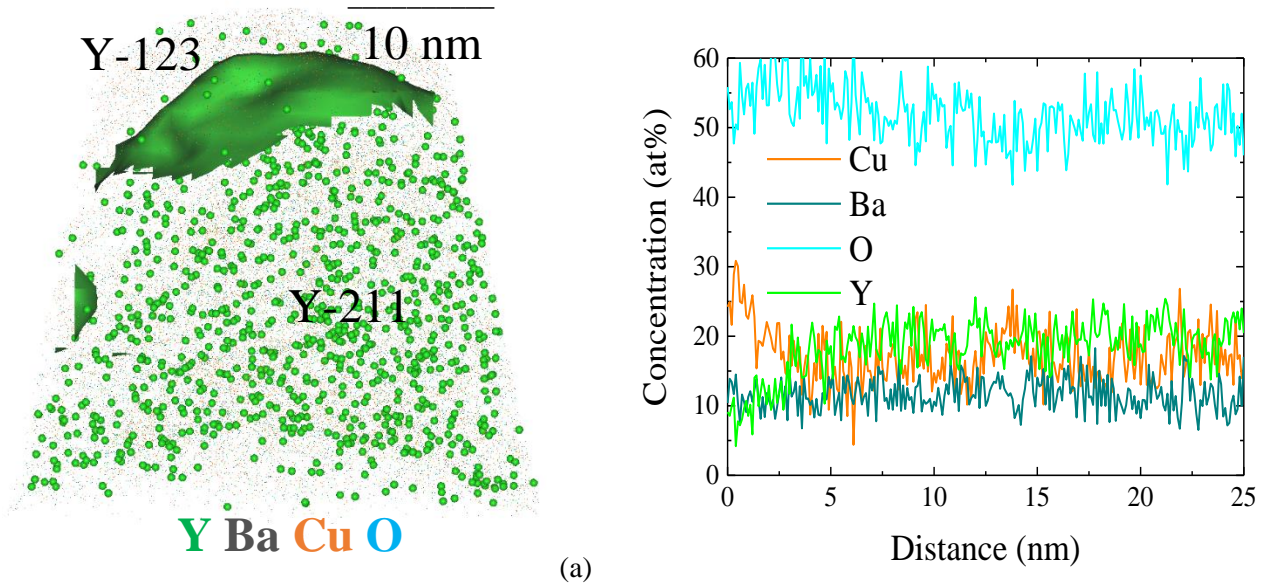
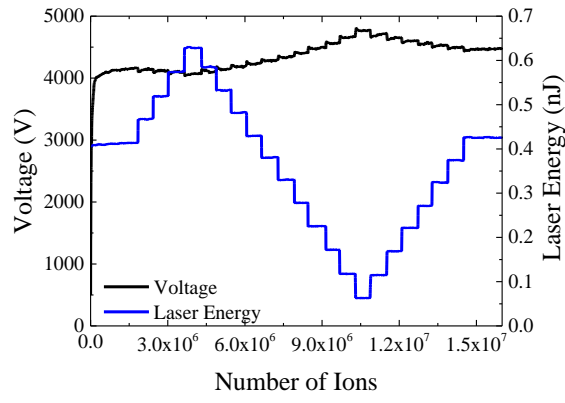
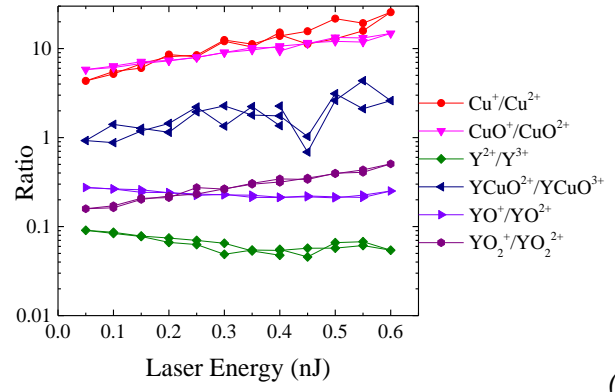


Figure 2: (a) Reconstruction of a sample containing a Y-211/Y-123 interface and (b) 1D concentration profile along the z -axis of the sample. Iso-concentration surface shown at 15 at.% Y highlights the position of the interface.



(a)



(b)

Figure 3: Selected laser energy and its effect on the experimental voltage required to field-evaporate ions at a constant detection rate from the atom probe needle during an experiment designed to study the effect of experimental running conditions on detected stoichiometry. (b) measured ionic charge state ratio as a function of applied laser energy.

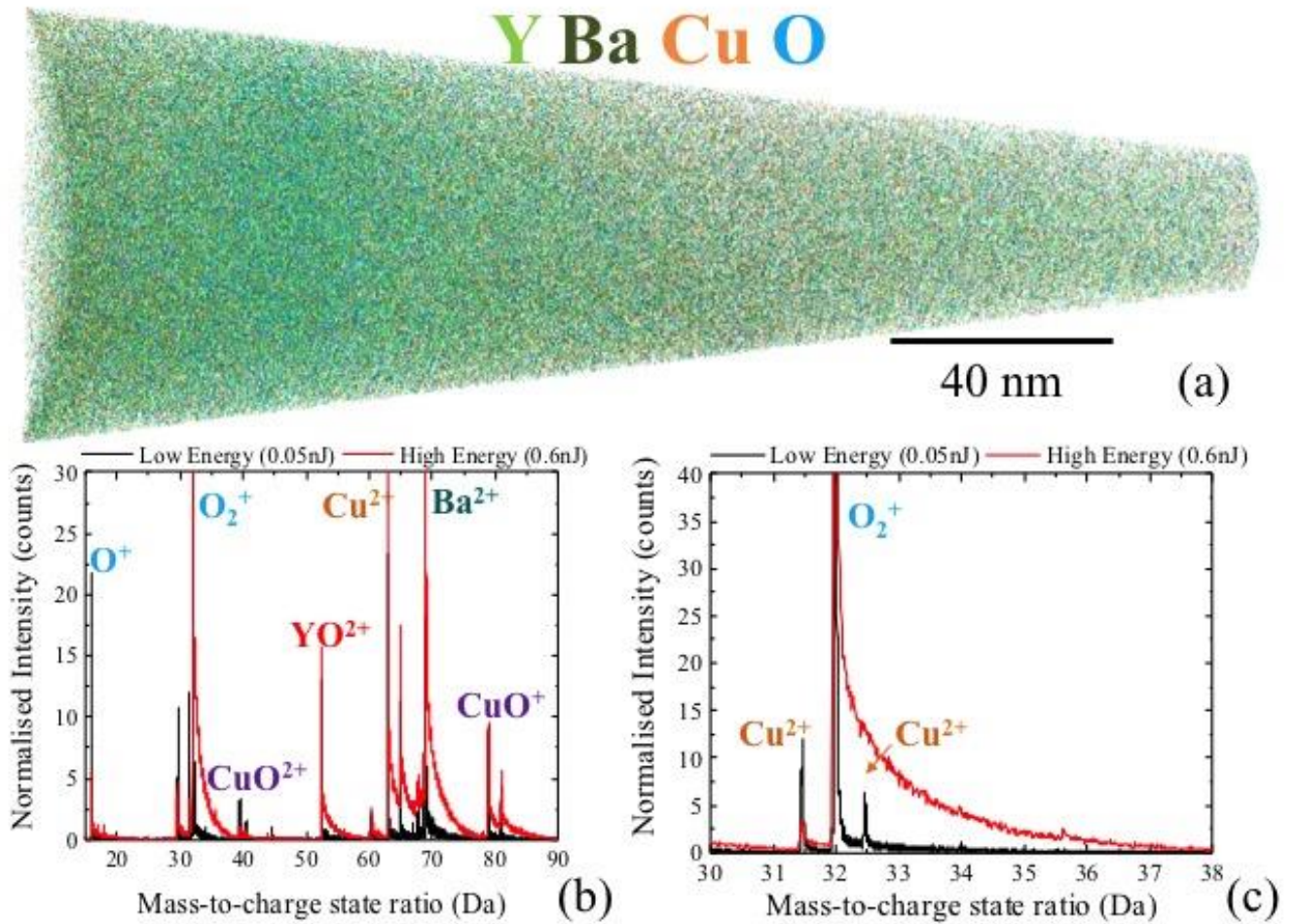
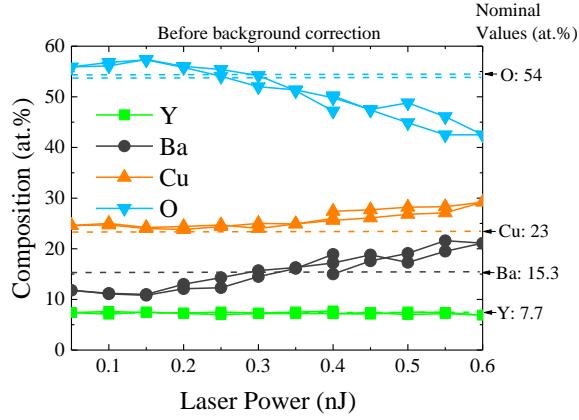
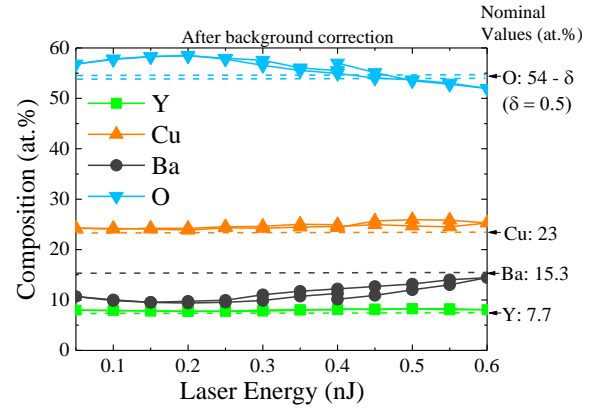


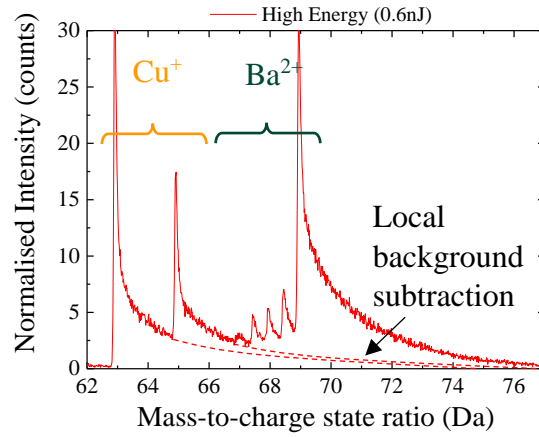
Figure 4: (a) Atom probe reconstruction of the YBCO needle showing a distribution of all ionic species and (b) mass spectra at the lowest and highest laser energies, 0.05 and 0.6 nJ, respectively, normalized using the highest peak (O_2^+) with some of the most prominent peaks labelled and (c) close-up of a section of the mass spectra illustrating the differences in resolution due to changing laser energy.



(a)



(b)



(c)

Figure 5: (a) composition variations with laser energy during an atom probe run of YBCO (peaks were ranged using full-width-half-maxima). The two values for each laser energy setting are a result of the analysis protocol shown in Figure 1. (b) Composition variation after background correction and (c) enlargement of the mass spectrum showing the barium-copper overlap which was resolved through an exponential fitting and subtraction of the copper peaks thermal tail contribution to the barium content.

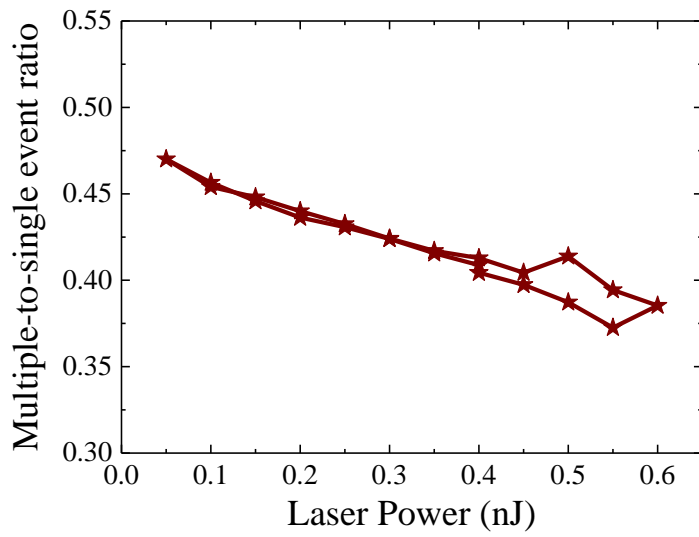


Figure 6: Ratio of multiple-to single events at different laser energies within an APT reconstruction of YBCO. The connecting line shows the acquisition sequence.

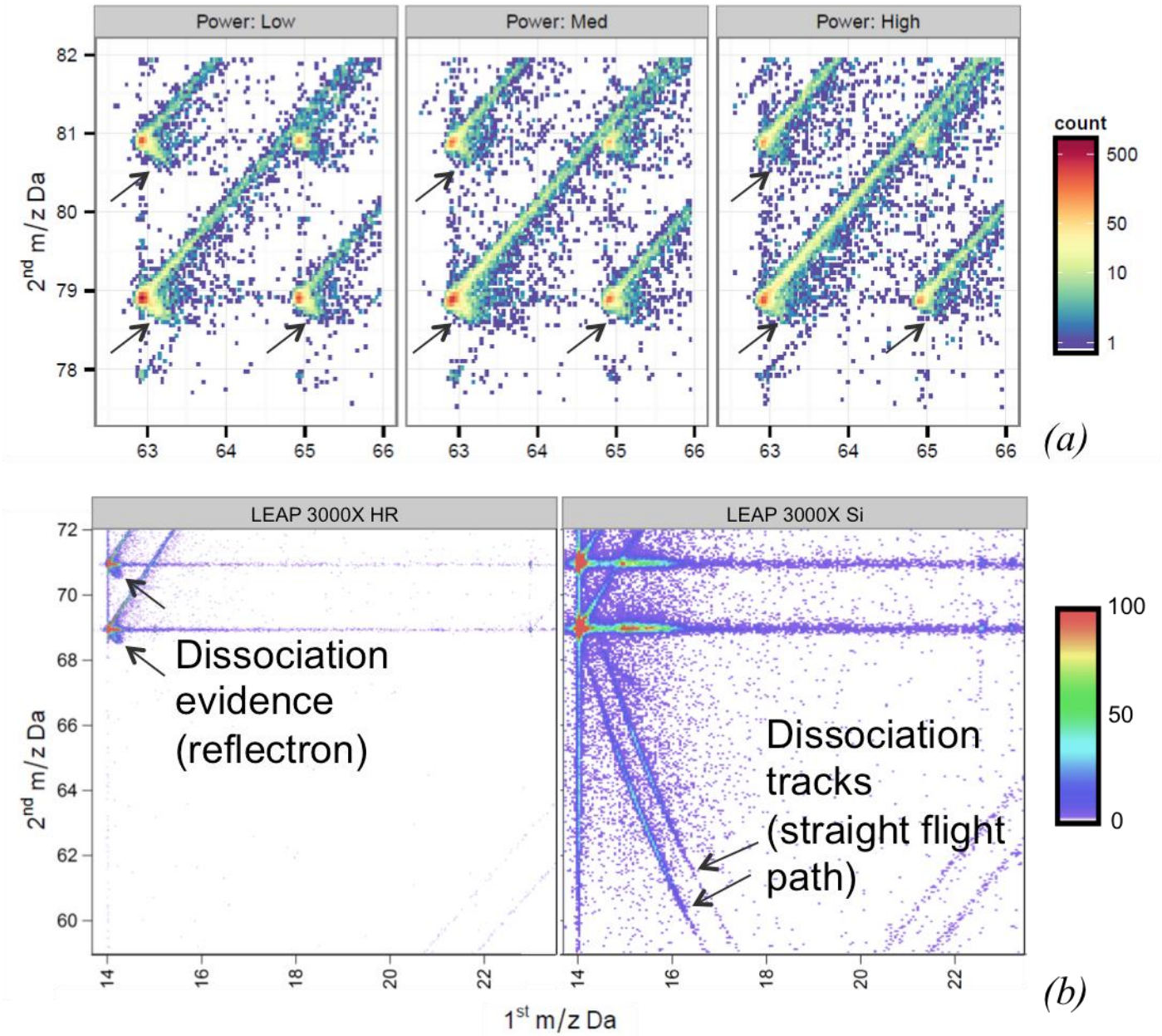


Figure 7: (a) Multiple hit correlation histograms showing an enlargement of the only area in which dissociation events were detected at different laser energies. The 1st event in this case is Cu^+ at 63 and 65 Da, the second is CuO^+ at 79 and 81 Da, which therefore indicates the dissociation of Cu_2O^{2+} ions. Lines with positive slope are expected in the mass spectrum of a specimen where no ion dissociation occurs. Any evidence of lines with a negative slope could be associated to dissociation events, as highlighted by the arrows. (b) comparison between a straight flight path local electrode atom probe (LEAP 3000 X Si) and a reflectron local electrode atom probe (LEAP 3000X HR) showing that an ellipsoidal trace with a negative slope in reflectron data can be indicative of substantial ion dissociation, the full tracks however can only be seen in straight flight path data. This data was acquired as part of a previous study on GaN samples.

References:

Babu, N. H., Jackson, K. P., Dennis, A. R., Shi, Y. H., Mancini, C., Cardwell, D. A., & Durrell, J. H. (2012). Growth of large size $\text{Y}_1\text{Ba}_2\text{Cu}_3\text{O}_7$ single crystals using the top seeded melt growth process. *Superconductor Science and Technology*, 25(7), 75012.

- Bachhav, M., Danoix, F., Hannoyer, B., Bassat, J.-M., & Danoix, R. (2013). Investigation of O-18 enriched hematite ($\alpha\text{-Fe}_2\text{O}_3$) by laser assisted atom probe tomography. *International Journal of Mass Spectrometry*, 335, 57–60.
- Badwal, S. P. S., Giddey, S., Munnings, C., & Kulkarni, A. (2014). Review of progress in high temperature solid oxide fuel cells. *Journal of the Australian Ceramic Society*, 50(1), 23–37.
- Benzi, P., Bottizzo, E., & Rizzi, N. (2004). Oxygen determination from cell dimensions in YBCO superconductors. *Journal of Crystal Growth*, 269(625), 2–4.
- Bunton, J. H., Olson, J. D., Lenz, D. R., & Kelly, T. F. (2007). Advances in pulsed-laser atom probe: instrument and specimen design for optimum performance. *Microscopy and Microanalysis*, 13, 418–127.
- Cerezo, A., Clifton, P. H., Lozano-Perez, S., Panayi, P., Sha, G., & Smith, G. D. W. (2007). Overview: recent progress in three-dimensional atom probe instruments and applications. *Microscopy and Microanalysis*, 13, 408–417.
- Cerezo, A., Grovenor, C. R. M., Hoyle, R. M., & Smith, G. D. W. (1988). Atom probe analysis of a ceramic oxide superconductor. *Applied Physics Letters*, 52(12), 1020–1022. <http://doi.org/10.1063/1.99232>
- Chen, D., Bishop, S. R., & Tuller, H. L. (2013). Nonstoichiometry in oxide thin films: A chemical capacitance study of the praseodymium-cerium oxide system. *Advanced Functional Materials*, 23(17), 2168–2174.
- Clifton, H., Gribb, T. T., Gerstl, S. S. A., Ulfig, R. M., & Larson, D. J. (2008). Performance advantages of a modern ultra-high mass resolution atom probe. *Microscopy and Microanalysis*, 14 (Suppl.), 454–455.
- Deconihout, B., Vurpillot, F., Gault, B., Da Costa, G., Bouet, M., Bostel, A., Blavette, Hideour, A., Martel, G., Brunel, M. (2007). Toward a laser assisted wide-angle tomographic atom-probe. *Surface and Interface Analysis*, 39, 278–282.
- Degardin, A. F., Galiano, X., Gensbittel, A., Dubrunfaut, O., Jagtap, V. S., & Kreisler, A. J. (2014). Amorphous Y-Ba-Cu-O oxide thin films: Structural, electrical and dielectric properties correlated with uncooled infrared pyroelectric detection performances. *Thin Solid Films*, 533, 104–108.
- Degoy, S., Jimenez, J., Martin, P., Martinez, O., Prieto, A. C., Chambonnet, D., Audry, C., Belouet, C., Perriere, J. (1996). Oxygen content of YBaCuO thin films. *Physica C: Superconductivity and Its Applications*, 256(3), 291.
- Gault, B., Moody, M. P., Cairney, J. M., & Ringer, S. P. (2012). *Atom Probe Microscopy*.
- Gault, B., Saxey, D. W., Ashton, M. V., Sinnott, S. B., Chiaramonti, A. N., Moody, M. P., & Schreiber, D. K. (2016). Behavior of molecules and molecular ions near a field emitter. *New Journal of Physics*, 18, 33031.
- Graf, T., Triscone, G., & Muller, J. (1990). Variation of the superconducting and crystallographic properties and their relation to oxygen stoichiometry of highly homogeneous YBa₂Cu₃O_x. *Journal of the Less – common Metals*, 159 C, 349.
- Hudson, D., Smith, G. D. W., & Gault, B. (2011). Optimisation of mass ranging for atom probe microanalysis and application to the corrosion processes in Zr alloys. *Ultramicroscopy*, 111, 480–486.
- Jia, C. L., Lentzen, M., & Urban, K. (2003). Atomic-resolution imaging of oxygen in perovskite ceramics. *Science*, 299, 870.
- Jorgensen, J. D., Hinks, D. G., Radaelli, P. G., Pie, S., Lightoot, P., Dabrowski, B., Segre, C. U., Hunter, B. A. (1991). Defects, defect ordering, structural coherence and superconductivity in the 123 copper oxides. *Physica C*, 184, 185–189.
- Kellogg, G. L., & Brenner, S. S. (1987). Field ion microscopy and imaging atom-probe mass spectroscopy

- of superconducting $\text{YBa}_2\text{Cu}_3\text{O}_{7-x}$. *Applied Physics Letters*, 51, 1851.
- Kelly, T. F., & Larson, D. J. (2000). Local Electrode Atom Probes. *Materials Characterisation*, 44, 59–85.
- Kelly, T. F., Vella, A., Bunton, J. H., Houard, J., Silaeva, E. P., Bogdanowicz, J., & Vandervoort, W. (2014). Laser pulsing of field evaporation in atom probe tomography. *Current Opinion on Solid State and Materials Science*, 18(2), 81–89.
- Kim, C. J., Kim, K.-B., Hong, G.-W., Won, D.-Y., Kim, B.-H., Kim, C.-T., ... Suhr, D.-S. (1992). Microstructure, microhardness, and superconductivity of CeO_2 -added Y–Ba–Cu–O superconductors. *Journal of Materials Research*, 7, 2349–2354.
- Kreisler, A. J., Jagtap, V. S., Sou, G., Klisnick, G., & Degardin, A. F. (2012). Semiconducting YBaCuO films grown on silicon substrates: IR room temperature sensing and fast pyroelectric response. *IOP Conference Series: Materials Science and Engineering*, 41(1), 12011.
- La Fontaine, A., Gault, B., Breen, A., Stephenson, L., Ceguerra, A. V., Yang, L., Nguyen, T. D., Zhang, J., Young, D. J., Cairney, J. M. (2015). Interpreting atom probe data from chromium oxide scales. *Ultramicroscopy*, 159(2), 354–359.
- Li, Q., Amemiya, N., Takeuchi, K., Nakamura, T., & Fujiwara, N. (2011). Effects of Unevenly distributed critical currents and damaged coated conductors to AC losses of superconducting power transmission cables. *IEEE Transactions on Applied Superconductivity*, 21(3), 953–956.
- Liu, F., & Tsong, T. T. (1984). Numerical calculation of the temperature evolution and profile of the field ion emitter in the pulsed-laser time-of-flight atom probe. *Reviews of Scientific Instruments*, 55(4), 1779.
- London, A., Lozano-Perez, S., Moody, M. P., Amirthapandian, S., Panigrahi, B. K., Sundar, C. S., & Grovenor, C. R. M. (2015). Quantification of oxide particle composition in model oxide dispersion strengthened steel alloys. *Ultramicroscopy*, 159(2), 360–367.
- Marquis, E. A., Araullo-Peters, V., Etienne, A., Fedotova, S., Fuji, K., Fukuya, K., Kuleshova, E., Legrand, A., London, A., Lozano-Perez, S., Nagai, Y., Nishida, K., Radiguet, B., Schreiber, D., Soneda, N., Thuvander, M., Toyama, T., Sefta, F., Chou, P. (2016). A Round Robin Experiment : Analysis of Solute Clustering from Atom Probe Tomography Data, 22(Suppl 3), 666–667.
- Melmed, A. J., Shull, R. D., Chiang, C. K., & Fowler, H. A. (1988). Possible evidence for superconducting layers in single crystal $\text{YBa}_2\text{Cu}_3\text{O}_{7-x}$ by field ion microscopy. *Science*, 239(176), 4836.
- Murakami, M., Gotoh, S., Fujimoto, H., Yamaguchi, K., Koshizuka, N., & Tanaka, S. (1991). Flux pinning and critical currents in melt processed YBaCuO superconductors. *Superconductor Science and Technology*, 4, 543–550.
- Nedeltcheva, T. (1995). Determination of oxygen stoichiometry in YBCO superconductors by spectrophotometry. *Analytica Chimica Acta*, 312(2), 223.
- Nedeltcheva, T., & Vladimirova, L. (2001). Spectrophotometric determination of oxygen stoichiometry in YBCO superconducting bulk samples. *Analytica Chimica Acta*, 437(2), 259.
- Nishikawa, O., & Nagai, M. (1988). Ultramicroanalysis of Y-Ba-Cu-O ceramics with the atom-probe microscope. *Physical Reviews B*, 37, 3685.
- Pinol, S., Sandiumenge, F., Martinez, B., Gomis, V., Fontcuberta, J., Obradros, X., Snoek, E., Roucau, C. (1994). Enhanced critical currents by CeO_2 additions in directionally solidified $\text{YBa}_2\text{Cu}_3\text{O}_7$. *Applied Physics Letters*, 65, 1448–1450.
- Saxey, D. (2011). Correlated ion analysis and the interpretation of atom probe mass spectra. *Ultramicroscopy*, 111(6), 437–479.
- Seh, H., Fritze, H., & Tuller, H. L. (2007). Defect chemistry of langasite III: Predictions of electrical and gravimetric properties and application to operation of high temperature crystal microbalance. *Journal*

- Suvorova, E. I., Cantoni, M., Buffat, P. A., Didyk, A. Y., Antonova, L. K., Troitskii, A. V., & Mikhailova, G. N. (2014). Structure analysis of the YBCO layer in Ag/YBCO/metal oxide buffer/Hastelloy composite tape before and after 107 MeV Kr¹⁷⁺ irradiation. *Acta Materialia*, 75, 71–79.
- Sykes, A., Gryaznevich, M. P., Kingham, D., Costley, A. E., Hugill, J., Smith, G., Buxton, P., Ball, S., Chappell, S., Melhem, Z. (2014). Recent advances on the spherical tokamak route to fusion power. *IEEE Transactions on Plasma*, 42(3), 482–488.
- Takeuchi, K., Amemiya, N., Nakamura, T., Maruyama, O., & Ohkuma, T. (2011). Model for electromagnetic field analysis of superconducting power transmission cable comprising spiraled coated conductors. *Superconductor Science and Technology*, 24(1), 85014.
- Tang, F., Gault, B., Ringer, S. P., & Cairney, J. M. (2010). Optimization of pulsed laser atom probe (PLAP) for the analysis of nanocomposite Ti-Si-N films. *Ultramicroscopy*, 110(7), 836–843.
- Thompson, K., Lawrence, D., Larson, D. J., Olson, J. D., Kelly, T. F., & Gorman, B. (2007). In situ site-specific specimen preparation for atom probe tomography. *Ultramicroscopy*, 107(2–3), 131–139.
- Tuller, H. L., & Bishop, S. R. (2011). Point defects in oxides: Tailoring materials through defect engineering. *Annual Review of Materials Research*, 41, 369–398.
- Vilalta, N., Sandiumenge, F., Pinol, S., & Obradors, X. (1997). Precipitate size refinement by CeO₂ and Y₂BaCuO₅ additions in directionally solidified YBa₂Cu₃O₇. *Journal of Materials Research*, 12, 1.
- Wu, K.-H., Hsieh, M.-C., Chen, S.-P., Chao, S.-C., Juang, J.-Y., Uen, T.-M., Gou, Y.-S., Tseng, T.-Y., Fu, C.-M., Chen, J.-M., Liu, R.-G. (1998). Preparation and Electronic Properties of YBa₂Cu₃O_x Films with Controlled Oxygen Stoichiometries. *Japanese Journal of Applied Physics*, 37, Part 1(8), 4346.